Eur. Phys. J. B **5**, 757–770 (1998)

THE EUROPEAN PHYSICAL JOURNAL B

Pattern formation in an inhomogeneous environment

W. Zimmermann[1,2,a], B. Painter[3], and R. Behringer[3]

[1] Institut für Festkörperforschung and FORUM Modellierung, Forschungszentrum Jülich, 52425 Jülich, Germany
[2] Max–Planck–Institute for Physics of Complex Systems, 01187 Dresden, Germany
[3] Department of Physics and Center for Nonlinear Science and Complex Systems Duke University, Durham NC, 27708-0305, USA

Received: 24 February 1998 / Revised: 19 May 1998 / Accepted: 23 June 1998

Abstract. A major step in understanding pattern formation has been achieved by studying idealized systems. However, in nature inhomogeneous systems are much more abundant than their idealized homogeneous counterparts. Here we report about experimental results on pattern formation in two inhomogeneous systems, thermal convection in porous media and Taylor-vortex flow between a rough and a smooth cylinder. Several aspects of heterogeneity effects in pattern formation are theoretically investigated for model equations and analytical descriptions are given for a few phenomena.

PACS. 47.20.-k Hydrodynamic stability – 47.54.+r Pattern selection; pattern formation – 71.55.-i Impurity and defect levels

1 Introduction

During recent decades, pattern formation has experienced enormous progress [1–5] and important insights were contributed by studies of idealized fluid systems such as Rayleigh-Bénard convection (RBC) [6], Taylor-Couette flow (TCF) [7] and electroconvection [8,9]. In many cases these experiments were carefully prepared and essentially homogeneous. Close to the onset of flow, there is now a general classification scheme of bifurcations and simple normal forms, so–called Ginzburg–Landau equations, provide a good qualitative description of some region near the onset of flow [4]. In fluid systems, quantitative understanding exists for many phenomena in pattern formation [4]. They are characterized by *control parameters*, which apply everywhere within the system. With increasing control parameter, ϵ, additional instabilities occur and lead to more and more complex spatio-temporal dynamics in these ideal systems. Typically, these complex flows are at best only partly understood, and are among the current challenges for dynamicists.

A much less studied issue is pattern formation in systems which are intrinsically inhomogeneous. In nature, pattern forming systems are in most cases inhomogeneous and their homogeneous isotropic counterparts are often prepared in laboratory experiments. An intrinsically inhomogeneous system is convection in porous media [10]. In fluid systems, as mentioned above, inhomogeneities may also arise from irregularities at the container boundaries. Often these irregularities are small compared to the extension of the fluid containers and the length scale of the pattern and the related effects are below the experimental resolution. However, in recent experiments, the size of the container has, in some cases, been considerably reduced and/or the experimental resolution strongly enhanced. Both effects make it more likely that roughness effects arise. These effects are unlikely to be explained by models assuming ideal flat boundaries. Here we describe experiments where irregularities are introduced in a controlled manner, either at the container boundaries or in the bulk. Such investigations allow a more systematic analysis of typical effects of irregularities. For instance, they allow an estimate of the robustness of phenomena which are usually studied under ideal conditions. But, the reduced symmetry and greater spatial complexity of inhomogeneous systems make them more difficult to study.

Linear waves, such as acoustic or electromagnetic waves in disordered media are already a subject extensively studied in recent years [11]. Perhaps most famous is Anderson localization, where disorder in a linear media causes an exponential decay of the transmission coefficient (see *e.g.* Refs. [11,12]). Nonlinearity may act counter to linear disorder effects, thus enhancing the transmission coefficient. Hence, solitons and spatially periodic patterns in model systems stay undistorted if nonlinearities are strong [13,14] .

A subclass of inhomogeneous systems are spatially periodic patterns which are spatially periodic modulated. These have been investigated already to some extent in one and two spatial dimensions. The competition between the wave length of the forcing and the naturally occurring

[a] *Present address*: Theoretische Physik, Universität des Saarlandes, 66041 Saarbücken, Germany.
e-mail: w.zimmermann@kfa-juelich.de

wave length of the pattern leads to a great variety of phenomena. In one spatial dimension it leads to commensurate/incommensurate transitions, phase solitons *etc.* [15–18] and in two spatial dimensions to complex patterns [19–21]. Single periodically forced systems and statistically heterogeneous systems share a number of common phenomena. For instance, in both cases the up-down symmetry can be broken and the bifurcation might be imperfect. However, it is a major difference between both that in heterogeneous systems the spectrum of forcing is broad. As discussed here, the broad spectrum may lead to localization effects and nonconstant weight for the wave lengths in the spectrum may lead to rounding of the bifurcation which is not mainly due to the imperfect bifurcation. Other heterogeneous and extensively investigated examples are coupled oscillators [22,23], where aspects of synchronization are in the focus of investigations and rough surfaces used for drag reduction (see *e.g.* [24]).

Here, we consider two spatially inhomogeneous systems experimentally. In Section 2 porous medium convection (PMC) and in Section 3 Taylor-Couette flow (TCF) where the inner cylinder is roughened by machining. In Section 4 effects of spatially varying coefficients are analyzed theoretically for one of the simplest models describing spatially periodic patterns, the Swift-Hohenberg model and effects of spatially varying boundaries in Rayleigh-Bénard convection.

2 Porous media convection (PMC)

We illustrate PMC in Figure 1, and discuss why PMC naturally falls into a class of intrinsically inhomogeneous nonlinear pattern forming systems. PMC is nominally similar to RBC, except that the region containing the fluid is shared with a solid medium. More specifically, the fluid resides in the open connected channels of a porous solid. If a thin horizontal layer of fluid-saturated porous medium is heated from below, leading to a temperature difference, ΔT, convection will occur if the porous Rayleigh number [10]

$$Ra = \alpha g \gamma d / \kappa \nu \tag{1}$$

exceeds a critical value. In the conventional picture of PMC as modeled by Darcy's law, $Ra_c = 4\pi^2$. Here, α, κ, ν and d are the appropriate thermal expansion coefficient, thermal diffusivity, kinematic viscosity and heights of the porous layer, and γ, defined below, is the permeability. At onset, the expected pattern is straight rolls of wavelength λ.

Although the conventional Darcian picture of PMC may give an approximate picture, it also assumes that the intrinsic structure of the medium is irrelevant. Recent experiments have shown that this structure can have a significant impact on pattern selection and heat transport [25–27]. It is this structure which can make a porous medium spatially inhomogeneous. In principle, one might construct an experiment for which the pore scale, δ, is arbitrarily small relative to the height of the porous layer, d. In this case the inhomogeneity resulting from the pores should be negligible. However, for conventional fluids like water, this is not really feasible. Here, we explore why that is the case by examining the conventional Darcy picture and its predictions. On some scale, a porous medium may be thought of as a continuum which, for slow flow speeds is characterized by Darcy's law:

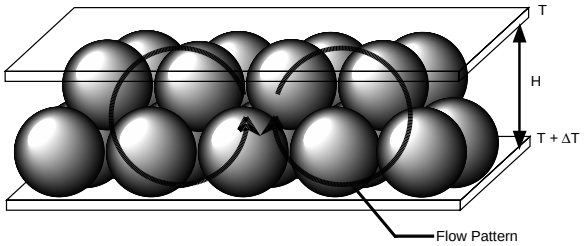

Fig. 1. Illustration of convection in a porous medium.

$$\mathbf{v} = -\gamma/\eta \cdot \nabla P. \tag{2}$$

Here, γ is the permeability and η is the shear viscosity. More sophisticated continuum descriptions exist, but they all share the assumption that there is a length scale, L, intermediate between the pore size, δ, and the overall system size, S, such that an average of the flow over a representative elementary volume (REV), $\sim L^3$, is described to a good degree of accuracy by Darcy's law. In a typical lab-scale system, the pore size cannot be made to satisfy the condition that $\delta \ll \lambda \simeq 2d$. This limitation arises because of two competing constraints. First, the pore size cannot be made very small, since otherwise, the temperature difference at and above onset is too large to have Boussinesq flow. Second, the height of the system cannot be made very large without incuring impractical relaxation times. The issue is captured in Figure 2. This figure shows the typical pore scale, δ *vs.* the layer height, d, with fluid parameters pertaining to water. Boussinesq convection can be obtained above the hyperbolic-like curve (assumes $\Delta T_c = 10\,\mathrm{K}$). Tractable relaxation times ($\tau = d^2/\kappa$) for vertical heat diffusion of less than 0.5 Hr apply below the horizontal line. And of course to be a sensible porous medium, we must have $\delta < d$.

The bottom line of this analysis is that although δ can be set less than d, the usual assumption, $\delta \ll d$ is hard to met. Therefore, there will be microscopic structure, which we can think of as local variation in R, with fluctuations on scales not too much smaller than the convective wavelength. Therefore, this system is a natural one for probing the effects of spatial fluctuations on *weakly nonlinear* pattern formation. Other systems have been studied which have slow spatial variations. Examples are TCF [29] and RBC with a spatial ramp [30] or RBC and EC with spatially single periodic boundary variations [16,31,32]. PMC is different in that inhomogeneities occur in the bulk and that the spectrum of spatial variations is broad and has significant strength at wave vectors larger (spatial scales smaller) than the characteristic system scale, $2\pi/d$. In our

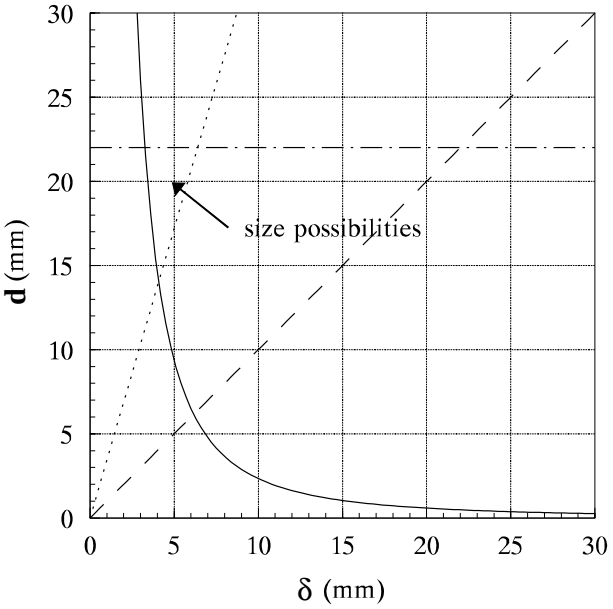

Fig. 2. Constraints for porous media convection (PMC), as represented by the pore scale, δ and the layer height, d. The hyperbolic-like curve applies for water, where $\Delta T = 10$ K at onset, assuming that this corresponds to Boussinesq convection. The region below this curve is non-Boussinesq. The horizontal line corresponds to a vertical thermal relaxation time of $\tau_v = 30$ min — roughly a maximal acceptable time. In addition, to be even remotely a porous medium, δ must be no larger than d, dashed line. A spatially homogeneous medium should satisfy $d/\delta \gg 1$ or alternatively $Da = \gamma/d^2 \ll 1$. If we choose $Da = 2 \times 10^{-5}$ then one must stay beyond the dotted line. When all these constraints are imposed, only the small triangular region remains as acceptable on all accounts. This region does not satisfy $\delta \ll d$.

examples, these variations may be either random or periodic.

The PMC experiments which we describe here were carried out using two rather different techniques, discussed in more detail in references [25–27]. Each technique is an experimental solution to the fact that in most cases, it is impossible to optically visualize the flow in porous media. This difficulty arises for several reasons. First, many porous media are not transparent. Second, even when the medium consists of transparent solid particles, differences in the indices of refraction of the fluid and solid plus the random curved or rough interfaces between the fluid and solid rapidly scatter the light. The first experiment described here uses specially constructed porous media for which there is a line of sight from above which is not affected by the problems above. Two types (out of an infinite collection of such materials) are sketched in Figure 3. One is spatially random (by design) and consists of randomly perforated, stacked, plastic sheets as shown in Figure 3a. The other is actually spatially periodic and is constructed by regular stackings of plastic bars, *cf.* Figure 3b [25,27].

The second experiment uses Magnetic Resonance Imaging (MRI), a noninvasive technique which can directly measure both the local fluid density and velocity [26]. Here, we present results for the vertical velocity. Each technique has advantages and disadvantages. The first is restricted to a subset of possible porous media, but can also yield very high precision data for the heat transport – Nusselt number Nu. The second can be used on virtually every medium (providing it is not magnetic or electrically conducting) but it is more difficult to obtain data for the heat transport.

Data from the first type of experiment, including the two different media are given in Figure 4. For the random medium shown in Figure 3a the fluid flow occurs *via* a cellular pattern which begins locally and with increasing R fills in the complete fluid layer, *cf.* Figure 4a.

This is also obvious from the Nusselt data which show a rounded transition, *cf.* Figure 4c. By contrast, the experiment constructed with a periodic stacking of bars with a rather small pore scale, *cf.* Figure 3b, shows an instrumentally sharp transition to convection, *cf.* Figure 4b,d. Thus, for the rather small pore scales of both media, $\delta < d$, the rounding in Nu in Figure 4c is clearly associated with the random spatial variations in the porous structure.

This is seen as well in the experiments using PMC. Here, we contrast in Figures 5, 6 data for a nominally random packing of spheres, a hexagonal packing of spheres in a rectangular container, and a hexagonal packing of spheres in a hexagonal container. In this sequence of different containers, we move from random to increasingly ordered structures. In the disordered packing, the flow starts in regions where there are defects in the packing (the source of the disorder), and with increasing ΔT convection fills the cell, similarly to the first case above. In the ordered packings, well defined convection rolls form instead, *cf.* Figure 6. In the case of the rectangular container, there is another interesting feature associated with local variations in Rayleigh number.

Note that packing spheres with a hexagonal pattern in a rectangular container means that along one pair of walls there will be a particularly large porosity/permeability and hence locally large Rayleigh number. In fact, convection does first start in this highest-γ region, although the small rolls which start there remain highly localized and do not seem to strongly affect the flow at higher values of the Rayleigh number.

3 Taylor-Couette flow with random spatial variations

A somewhat simpler example of a system with random spatial variations is a conventional Taylor–Couette (TCF) apparatus as shown in Figure 7 [7], for which the gap size is variable as indicated in Figure 8. In our experiment [28] the inner cylinder has been roughened by machining axisymmetric grooves along the length of the cylinder. The location of the grooves is random by design, and the spectrum of wavelengths, Figure 8, is roughly flat up to the wavenumber corresponding to the axial width of the grooves. The inner surface of the outer cylinder is smooth, so that the grooves in the inner cylinder uniquely impart random axial variation in the Taylor number.

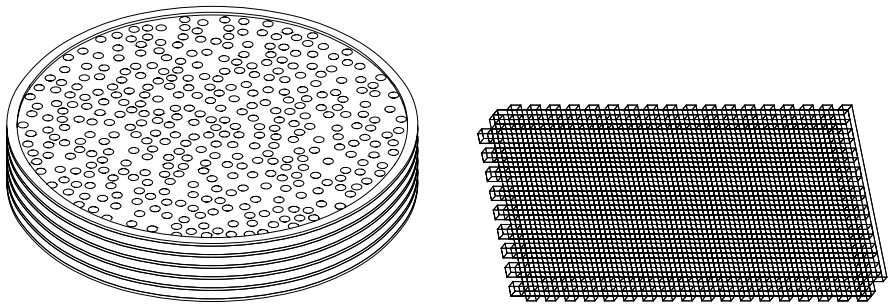

(a) (b)

Fig. 3. Specially constructed porous media.

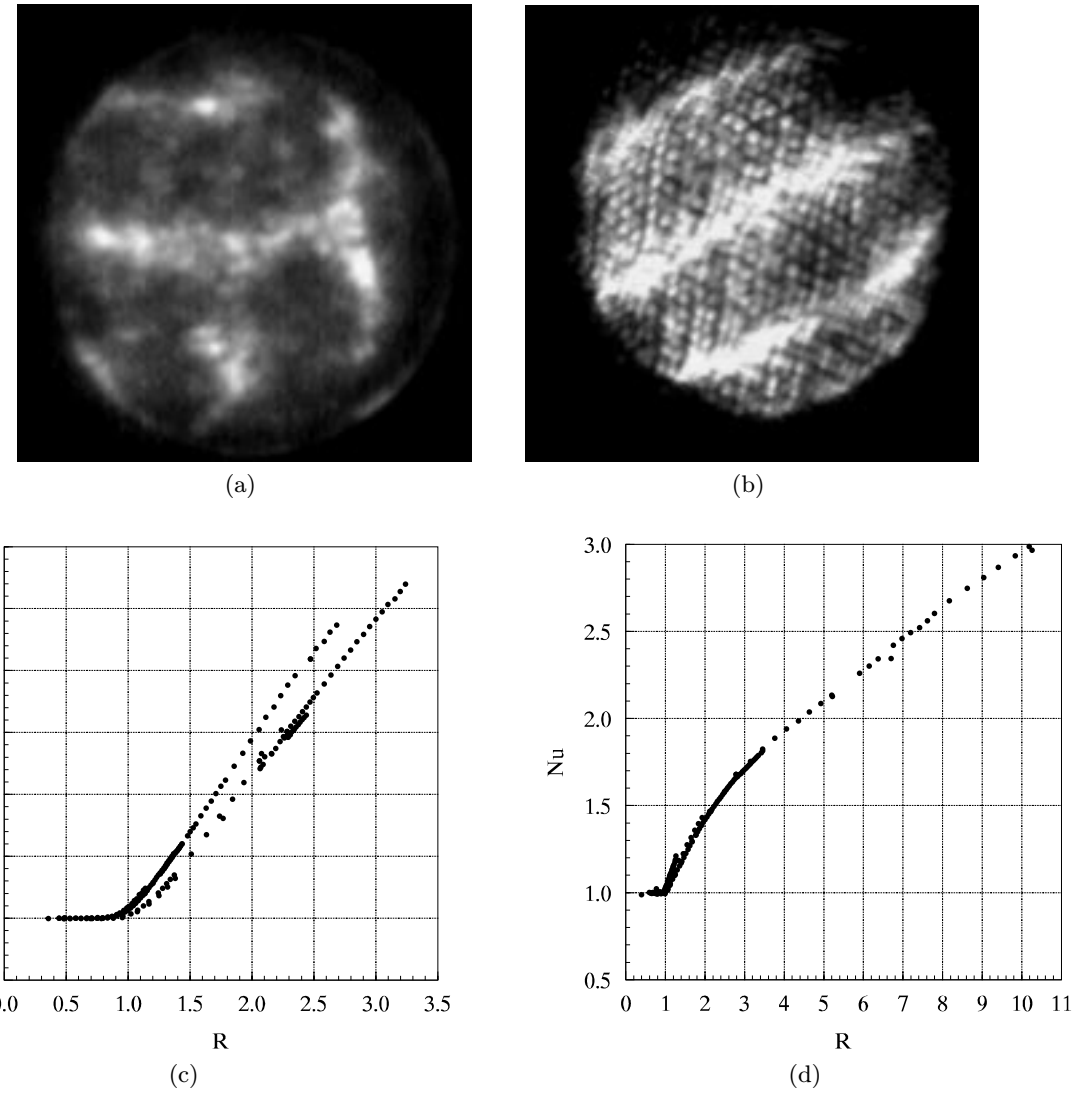

(a) (b) (c) (d)

Fig. 4. In (a) a typical pattern observed for random medium is shown, *cf.* Figure 3a, and in (b) a typical pattern observed for a rectangular grid porous medium, *cf.* Figure 3b. In (c) and (d) the respective data for the heat transfer (Nusselt number Nu) are shown as function of the reduced Rayleigh-number $R = Ra/Ra_c$.

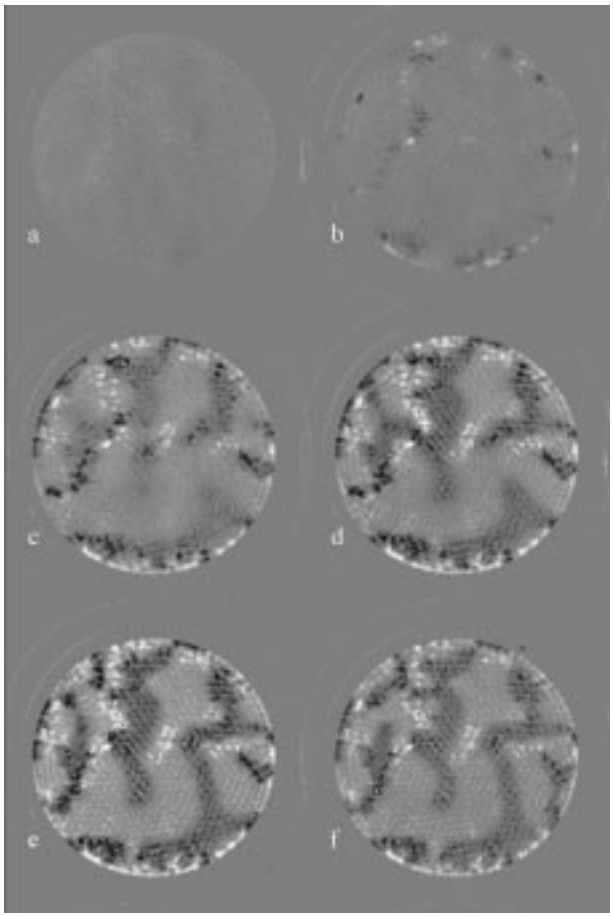

Fig. 5. Vertically averaged, vertical velocity for a circular cell with disordered packing of spheres. In (a) for a vanishing temperature difference between the top and bottom boundary, $\Delta T = 0.0$. From part (b) to (f) the velocity pattern is shown for different values of the reduced temperature difference, $\varepsilon = (\Delta T - \Delta T_c)/\Delta T_c$. (b) $\varepsilon = -0.5$, (c) $\varepsilon = 1.0$, (d) $\varepsilon = 3.0$, (e) $\varepsilon = 5.0$ and (f) $\varepsilon = 3.0$, but after first decreasing ΔT to 0 and then raising it back to 3.0.

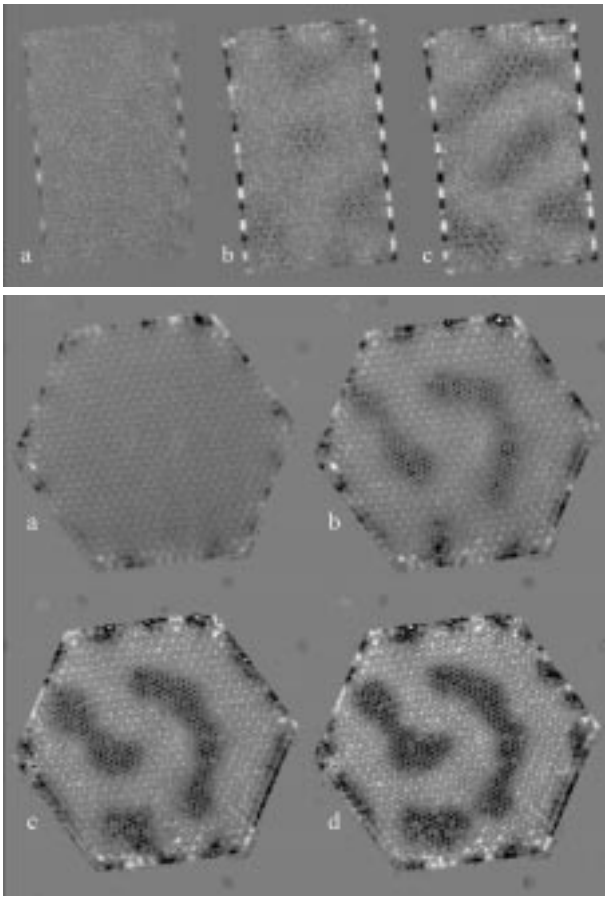

Fig. 6. Vertically averaged, vertical velocity for a packing of the spheres with hexagonal symmetry. Top: Rectangular container for different values of the reduced temperature (a) $\varepsilon = -0.5$, (b) $\varepsilon = 0.2$ and (c) $\varepsilon = 0.4$. Bottom: For a hexagonal cell at different values of ε below and above critical.

Unlike earlier experiments on fluid flow in containers with boundary variations, such as ramps [29,30] or spatially periodic variations [16,32], the experiment we consider here is similar in character to PMC in that the variations are random and have a broad spectrum with a significant power for wavelengths less than d.

In order to characterize the effect of spatial variability in Reynolds number Re,

$$Re = \frac{\Omega_1 R_1 (R_2 - R_1)}{\nu}, \tag{3}$$

it is important to measure the local velocity field throughout the experiment. We do so by particle imaging velocimetry (PIV). The fluid is seeded with a very low density of Kalariscope particles and then imaged with a short depth-of-field using a small CCD camera mounted on a stage which we transport vertically. The field of view is restricted to the outer 1/4 of the fluid, and from computer analysis of the particle tracks, we obtain the vertical velocity. For example, Figure 9 shows a representative example of the tracks generated by particles, and Figure 10 shows an example of the vertical velocity field v of Taylor vortices for a smooth inner cylinder.

The velocity measurements with the rough inner cylinder show clearly the effects of localization of the flow, Figure 10. The initial flow clearly occurs in the regions of locally largest Re which is intuitively obvious. With increasing Ω_1, the flow spreads to other regions of the fluid and the localization becomes weaker, as indicated by the decreasing width of the power spectrum for the Taylor vortices.

For homogeneous systems, the bifurcation of the pattern, here the Taylor vortices, is characterized either by the Re-dependence of the local vertical velocity at a fixed position or by the Re–dependence of the spatially (axially) averaged velocity $\langle v^2 \rangle$. For inhomogeneous systems, such as for a rough inner cylinder, the functional dependence of the vertical velocity v on Re will change with the position of the measurement. Hence it is more appropriate to characterize the bifurcation by the averaged velocity $\langle v^2 \rangle$, as done in Figure 11. Moreover the deviation between the local and the global measurement is expected to be

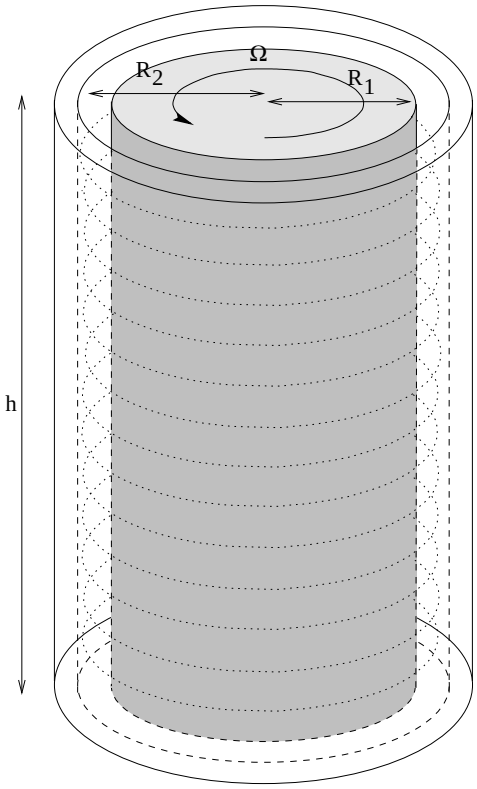

Fig. 7. The conventional Taylor-Couette apparatus is shown. The gap between the two cylinders at R_1 and R_2 is filled with water and the inner cylinder is rotated. Beyond a critical angular frequency Ω_1 the linear shear profile (Couette flow) becomes unstable and periodic Taylor vortices occur (see *e.g.* [7]).

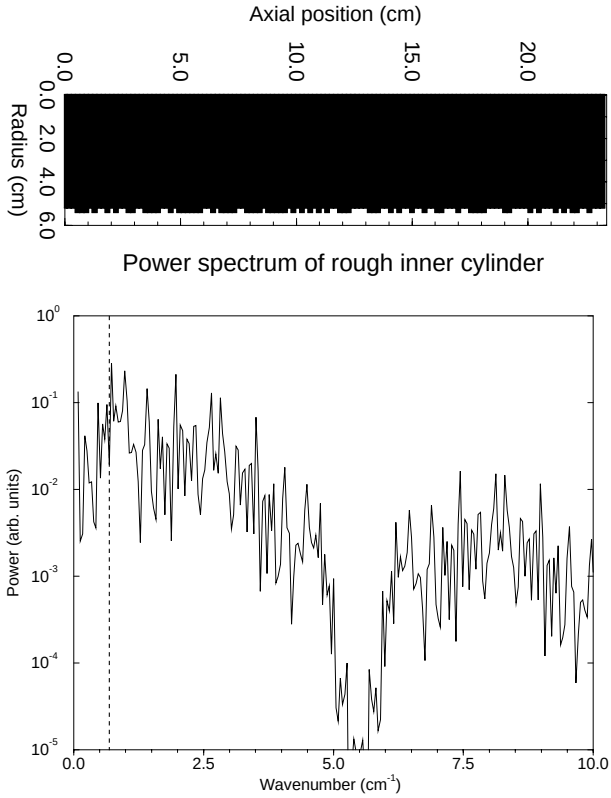

Fig. 8. The top part shows half of the rough inner cylinder of the TCF apparatus. The figure at bottom gives the power spectrum related to the roughness of the inner cylinder, whereby the dashed line corresponds to the wavenumber of the Taylor vortices without the roughness.

correlated with the localization of the pattern. Both should decrease with increasing values with increasing amplitude of the velocity of the vortices.

Since no *ab-initio* calculation for the Taylor system with a rough inner cylinder is yet available, it is interesting to ask which generic model best fits the measurements. Inspection of the power spectrum of the roughness, *cf.* Figure 8, tells us that the wave number at the first peak, q_{n1}, is close to the critical wave number q_c of the Taylor vortices. Hence, one expects a resonance $1:1 = q_c/q_{n1}$, which can be described by an appropriate Ginzburg–Landau-equation with an additive constant [31,34]. In the power spectrum in Figure 8 there are also strong contributions at larger wave numbers. Therefore, there could also be higher order resonance effects, such as $1:2$, $1:3$ and $1:4$ resonances. The modification of a supercritical bifurcation according to such resonances has been described by Coullet [17]. For a $1:2$ and a $1:4$ resonance the former supercritical bifurcation is still sharp. A $1:2$–resonance just shifts the threshold to smaller values and the $1:4$ reduces the prefactor β in the bifurcation relation $v^2 = \beta\epsilon$. Assuming that the rounded bifurcation in Figure 11 is mainly due to these resonant contributions of the power spectrum of the roughness, the part of the spectrum contributing to the $1:1$ and the $1:3$ resonance can primarily induce the rounding. Both resonances have been considered separately for single periodic forcing in reference [17].

Accordingly, the model describing both resonances simultaneously reads as

$$\partial_t A = \epsilon A + bA^2 - cA^3 + h, \tag{4}$$

if any spatial dependence is neglected. The solid line in Figure 11 correspond to a least squares fit to the stable steady solutions of this model. The quality of the fit is fair. Even a nearly exponential law in an intermediate range is fitted by the algebraic rule for this simple imperfect bifurcation.

We contrast the data for the rough inner cylinder with data for a nearly ideal experiment, *cf.* Figure 11. Within experimental resolution we see a sharp bifurcation (the Eckmann vortices visible in Figure 10 represent a weak imperfection in this case). Moreover, the data for $\langle v^2 \rangle$ are well fitted by a linear function of Re.

The model of equation (4) completely neglects the influence of wave numbers in the power spectrum, aside from $1:1$ and $1:3$ resonances. However, the other contributions are crucial to explain localization of velocity field as shown in Figure 10. Localization effects are only expected for a perturbation with a broad spectrum, never for single periodic resonant forcing.

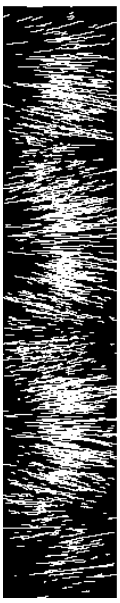

Fig. 9. Particle tracks in Taylor Couette Flow.

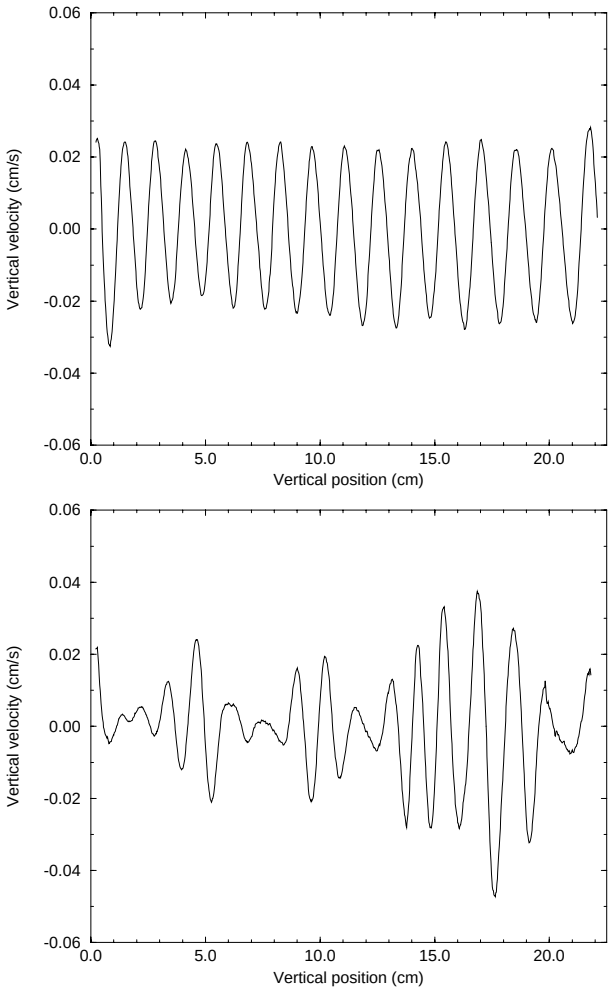

Fig. 10. Vertical velocity field of Taylor vortices with a smooth inner cylinder (top) and for the rough inner cylinder as shown in Figure 8 (bottom).

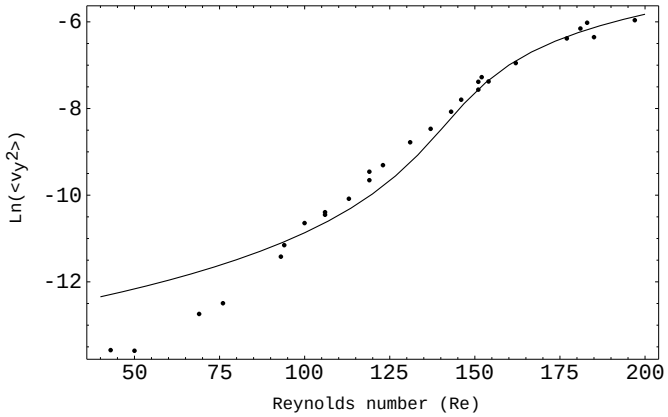

Fig. 11. The spatially averaged and squared axial velocity $log(\langle v^2 \rangle)$ is shown as function of the Reynolds number $Re = \Omega_1 R_1 (R_2 - R_1)/\nu$, dots, and the solid line is a fit with the model given in equation (4).

Usually, rounding of the bifurcation as shown in Figure 11 is interpreted as an imperfect bifurcation as it is met for instance close to a 1 : 1 resonance. However, it has been shown by a numerical study of the Swift–Hohenberg equation with a random perturbation of the control parameter, that one can have both, such a rounded bifurcation and a sharp threshold for the onset of the pattern simultaneously [14]. This and other theoretical aspects of random perturbations are discussed in the next Section 4.

4 Simple models for inhomogeneities in pattern formation

Thermal convection has been theoretically investigated for inhomogeneous conditions. For spatial variations at the container boundaries [30–32,34–36] (including modulations in a rotating cylindrical annulus [33]), for a weakly heterogeneous porous medium [37] and for homogeneous porous media with boundary imperfections [38–41]. For these examples, well established equations of motion are available and approximately solved, whereby contributions in the disorder spectrum are emphasized, which are in 1 : 1 resonance with the spatial periodicity of the pattern. This type of resonance induces an imperfect bifurcation and hence leads to a rounded bifurcation shape. However, the broad wave number spectrum of heterogeneities is crucial for a number of disorder effects. An example is localization of the pattern, which is absent for single periodic forcing. Localization of a pattern has been shown for the Swift–Hohenberg equation with a random contribution to the control parameter [14].

The Swift–Hohenberg equation is one of the simplest models describing a bifurcation from a homogeneous initial state to a stationary and spatially periodic pattern [4,42]. For this model, the bifurcation is sharp but rounded. That is, the no-flow state exists and is stable up to a critical value of the control parameter, and above the bifurcation, the dependent field shows upward curvature. Here we show by a perturbational calculation that

this rounding is partly due to nonresonant contributions in the spatially varying control parameter. In a further section we emphasize that spatially varying drifts induce a time dependence of spatially periodic patterns.

4.1 Swift–Hohenberg with spatially varying control parameter

In this section a generalized Swift–Hohenberg model is studied, which has a broken spatial translational symmetry. This system,

$$\partial_t u = \left[\varepsilon + M_1(x) - (q_0^2 + \partial_x^2)^2\right] u - u^3 + M_3(x), \qquad (5)$$

was discussed first in reference [14]. ε is the control parameter that is similar to the reduced Taylor or Rayleigh number in real systems, and q_0 is the critical wave number at threshold of the unperturbed case, $M_i = 0$.

Various perturbations affect the pattern selection in this system in different ways. A spatially and single periodic perturbation $M_1(x)$, with a modulation wave number k_1 of the order of the wave number of the pattern, q_0, leads to commensurate/incommensurate transitions in one spatial dimension [17,43] and to a new pattern in two spatial dimensions [20,21]. A random function $M_1(x)$ leads to localization of the pattern and to a rounding of the bifurcation, which is still sharp [14]. An additive function $M_3(x)$ breaks the $\pm u$-symmetry in equation (5). In two spatial dimensions this broken symmetry forces hexagonal patterns. Thermal fluctuations are a function of space and time and occur also additively, such as $M_3(x,t)$.

Numerical calculations of equation (5) have shown for $M_3(x) = 0$ that the bifurcation from the basic state, $u \equiv 0$, is still sharp, but shifted to lower values [14]. In addition the Nusselt number

$$N(\varepsilon) = \frac{1}{L}\int_0^L dx\, u(x)^2 \qquad (6)$$

as function of the control parameter, ε, has a rounded shape similar to an imperfect bifurcation [31].

If we assume a small modulation, $M_1(x) = \eta \bar{M}_1(x) \propto O(1)$ ($\eta \ll 1$) then the threshold shift as well as the rounding of the bifurcation can be calculated by a perturbational calculation as indicated in the following two sections.

4.1.1 Threshold shift - $M_3(x) = 0$

We expand the control parameter as well as the solution of the linear part of equation (5) in powers of the modulation strength η:

$$\varepsilon_c = \varepsilon_c^{(0)} + \eta\varepsilon_c^{(1)} + \eta^2\varepsilon_c^{(2)} + \dots, \qquad (7)$$
$$u(x) = u_0(x) + \eta u_1(x_) + \eta^2 u_2(x) + \dots \qquad (8)$$

With the definition of the linear operator,

$$\mathcal{L}_0 = \varepsilon_c^{(0)} - (q_0^2 + \partial_x^2)^2, \qquad (9)$$

the following hierarchy of equations is obtained from equation (5):

$$\eta^0: \quad \mathcal{L}_0 u_0 = 0, \qquad (10)$$
$$\eta^1: \quad \mathcal{L}_0 u_1 = -[\bar{M}_1(x) + \varepsilon_c^{(1)}]u_0, \qquad (11)$$
$$\eta^2: \quad \mathcal{L}_0 u_2 = -[\bar{M}_1(x) + \varepsilon_c^{(1)}]u_1 - \varepsilon_c^{(2)} u_0. \qquad (12)$$

From these equations, threshold shifts can be calculated at the respective orders $\varepsilon_c^{(1)}, \varepsilon_c^{(2)}$. The final expressions are in general lengthy and depend on the choice of the stochastic properties of $\bar{M}_1(x)$. However, the essential features can be demonstrated with a periodic perturbation,

$$\bar{M}_1(x) = 2\bar{G}\cos(kx). \qquad (13)$$

If we start with an unperturbed solution,

$$u_0(x) = A_0\cos(q_1 x), \qquad (14)$$

then we obtain $\varepsilon_c^{(0)} = (q_0^2 - q_1^2)^2$ from the marginal stability condition equation (10).

No resonance $k \neq 2q_1$

When the external modulation is not in resonance with the pattern, then the product $\bar{M}_1(x)u_0$ includes no contribution proportional to the unperturbed solution, u_0. In this case the first order equation (11) can be solved for $\varepsilon_c^{(1)} = 0$:

$$u_1(x) = -\left(\frac{\bar{G}\cos((q_1+k)x)}{\varepsilon_c^{(0)} - (q_0^2 - (q_1+k)^2)^2} + \frac{\bar{G}\cos((q_1-k)x)}{\varepsilon_c^{(0)} - (q_0^2 - (q_1-k)^2)^2}\right) A_0. \qquad (15)$$

In equation (12), the product $\bar{M}_1(x)u_1(x)$ includes a contribution proportional to $u_0(x)$ and $u_0(x)$ belongs to the kernel of the operator $\mathcal{L}_0$. At the right hand side in equation (12) the part $\propto u_0(x)$ vanishes only when

$$\varepsilon_c^{(2)} = \frac{\bar{G}^2}{\varepsilon_c^{(0)} - (q_0^2 - (q_1+k)^2)^2} + \frac{\bar{G}^2}{\varepsilon_c^{(0)} - (q_0^2 - (q_1-k)^2)^2}, \qquad (16)$$

which gives the threshold shift in second order. This expression simplifies to

$$\varepsilon_c^{(2)} = -\frac{\bar{G}^2}{k^2}\left(\frac{1}{(2q_0+k)^2} + \frac{1}{(2q_0-k)^2}\right) \qquad (17)$$

when the wavelength is adjusted at the minimum of the unperturbed threshold, $q_1 = q_0$. For small wave numbers $k \ll q_0$, this expression becomes even more compact:

$$\varepsilon_c^{(2)} = -\frac{2\bar{G}^2}{4\,q_0^2\,k^2}\,. \qquad (18)$$

Hence a spatially periodic modulation (13) reduces the threshold for the bifurcation, whereby a divergence occurs in equation (17) both for $k \to 0$ and $k \to 2q_1$. The latter resonant case is now considered separately.

Resonance $k = 2q_1$

Here, the product $\bar{M}_1(x)u_0$ on the right hand side of equation (11) includes a contribution proportional to u_0 and equation (11) can be fulfilled only when $\varepsilon_c^{(1)} = -\bar{G}$. For this resonant case, the solution $u_1(x)$ includes only the first contribution of the expression in equation (15), and the whole expression for the threshold ε_c is given by

$$\varepsilon = \varepsilon_c^{(0)} - \eta\bar{G} - \eta^2 \frac{\bar{G}^2}{\varepsilon_c^{(0)} - (q_0^2 - 9q_1^2)^2} + \dots \qquad (19)$$

This short calculation shows that the threshold is shifted linearly by contributions to $\bar{M}_1(x)$ which are resonant to the pattern $k = 2q_1$ and that the shift is quadratic otherwise.

4.1.2 Rounding of the bifurcation – $M_3(x) = 0$

For the homogeneous case, $M_1 = 0$, the Nusselt–number N in equation (6) increases linearly with ε beyond threshold. Here we address the question of how $N(\varepsilon)$ is modified by a spatially periodic and nonresonant modulation as given in equation (13). The technical steps become simpler for a long wave length modulation $k \ll q_0$. In this limit, the Swift–Hohenberg equation reduces further to an amplitude equation (see Appendix B of Ref. [4]) with a spatially periodic coefficient,

$$\partial_t A = \Big[\varepsilon + M_1(x) + 4q_0^2\partial_x^2 - 3 \mid A \mid^2 \Big] A, \qquad (20)$$

and with $u(x,t) = A(x,t)\exp(iq_0x) + A^*(x,t)\exp(-iq_0x)$. Repeating the steps of the perturbation expansion for the Swift–Hohenberg equation in Section 4.1.1, one finds again the threshold shift for a long wavelength modulation as given in equation (18). Equation (20) has for $M_1 = 0$ a constant solution $A^2 = \varepsilon/3$. We assume again small modulation amplitudes $M_1(x) \propto \eta$ and we calculate the corrections to this constant nonlinear solutions:

$$A = \frac{1}{\sqrt{3}}\Big[A_0 + \eta A_1 + \eta^2 A_2 \dots\Big]. \qquad (21)$$

With this ansatz we expand equation (20) with respect to powers of the small parameter η and we obtain:

$$\eta^0 : (\varepsilon + 4q_1^2\partial_x^2)A_0 - \mid A_0 \mid^2 A_0 = 0, \qquad (22)$$

$$\eta^1 : (\varepsilon + 4q_1^2\partial_x^2)A_1 - A_0^2\,(2A_1 + A_1^*) = -2\bar{G}\cos(kx)A_0, \qquad (23)$$

$$\eta^2 : (\varepsilon + 4q_1^2\partial_x^2)A_2 - A_0^2\,(2A_2 + A_2^*) = -2\bar{G}\cos(kx)A_1 + A_0\left(A_1^2 + 2 \mid A_1 \mid^2\right). \qquad (24)$$

The solution of equation (23) is

$$A_1 = \frac{2\bar{G}A_0}{4q_1^2k^2 + 2\varepsilon}\ \cos(kx) = B_1\cos(kx), \qquad (25)$$

which vanishes in the limit of large values of ε such as $1/\sqrt{\varepsilon}$. The spatially independent contribution to A_2 is

$$\tilde{A}_2 = \frac{A_0}{\varepsilon}\frac{\bar{G}^2(4q_1^2k^2 - \varepsilon)}{(4q_1^2k^2 + 2\varepsilon)^2}\,. \qquad (26)$$

These solutions A_i allow an expansion of Nusselt number up to the leading orders, and one has

$$N = 2 \mid A \mid^2 = \frac{2}{3}\Big[A_0^2 + \eta^2(B_1^2/2 + A_0\tilde{A}_2) + \dots\Big] = \frac{2}{3}\Big[\varepsilon + 2\eta^2\frac{\bar{G}^2\,q_1^2k^2}{(2q_1^2k^2 + \varepsilon)^2}\dots\Big]. \qquad (27)$$

The Nusselt number is already finite at the threshold for the unperturbed SH-equation, $\varepsilon = 0$ and at threshold of the perturbed problem, $\varepsilon \propto -\eta^2$, ε in the denominator can be neglected and N vanishes precisely at the shifted threshold given in equation (18). Far beyond threshold the Nusselt number approaches the linear ε–dependence of the unperturbed situation. The initial slope of N,

$$\frac{\partial N}{\partial\varepsilon}(\varepsilon = \varepsilon_c) = \frac{2}{3}\Big[1 - 8\eta^2\frac{\bar{G}^2}{16q_1^4k^4}\dots\Big], \qquad (28)$$

is reduced by the external perturbation. This reduction of the initial slope and the vanishing correction for the Nusselt number at larger values of ε indicate the rounding of $N(\varepsilon)$, as can easily be seen by plotting the expression (27) as a function of ε. Calculations for a perturbation $M_1(x)$ with a broad power spectrum lead to qualitatively similar results. This ε–dependent slope of $N(\varepsilon)$ is an analytical explanation of the numerically obtained rounding of the sharp bifurcation in reference [14]. Hence, not only $1:1$ resonance leads to rounding of the bifurcation. The effects on the Nusselt-number discussed here are proportional to A^2. Hence the corrections are $\propto \eta$ close to $1:2$–resonance and $\propto \eta^2$ out of resonance. Whether the resonant or nonresonant corrections dominate, depends on the wave number distribution of disorder and on the value of the control parameter ε. This issue will be discussed in more detail elsewhere.

4.2 Effects of spatially varying drifts

It has been shown for a Rayleigh–Bénard experiment in reference [32] that a simultaneous modulation of the top and bottom container boundary leads to drifting convection rolls when the modulation wavelength is the same at the top and bottom and when both modulations are phase shifted relative to each other. This situation has been generalized to modulations of the top and bottom boundary with different wave lengths [21,44], and a so–called *Hopf–bifurcation by frustrated drifts* has been predicted for such an inhomogeneous situation.

The simplest pattern forming model describing the effects induced by frustrated drifts, is the Swift-Hohenberg equation with a spatially varying drift coefficient $M_2(x)$:

$$\partial_t u = \big[\varepsilon - (q_0^2 + \partial_x^2)^2 + M_2(x)\partial_x\big]u - u^3. \qquad (GSH) \qquad (29)$$

A constant drift, $M_2(x)\partial_x$, with $M_2(x) = const.$, can be removed by transforming into the comoving coordinate frame $x \to x + Mt$. For a spatially periodic modulation, $M_2(x)$, with vanishing spatial mean value, $\int dx\, M_2(x) = 0$, the local drifts are *frustrated*. Above some critical amplitude of $M_2(x)$, the bifurcation from the trivial state, $u \equiv 0$, is oscillatory and one finds the so–called *Hopf bifurcation by frustrated drifts* [45,46]. If, for instance, $M_2(x)$ is the sum of two harmonic functions, then even a fourfold degenerated Hopf–bifurcation might occur [46].

Next, we assume that $M_2(x)$ is harmonic and we consider the following two explicit forms:

$$M_2(x) = 2G_2 \cos(2kx + \varphi), \tag{30}$$

$$M_2(x) = 2G_2 \cos(4\hat{k}x + \varphi) + 2G_3 \cos(6\hat{k}x + \varphi_2). \tag{31}$$

The first expression is periodic with respect translations $x \to x + \pi/k$, and the second one, given in equation (31), is periodic with respect to $x \to x + \pi/2\hat{k}$. In order to keep the results comparable later on, we choose $k = 2\hat{k}$. Stochastic drifts as well as a stochastic contribution in the control parameter ε are discussed elsewhere in more detail [14].

Because of the periodicity of $M_2(x)$, the solutions of the linear part of equation (29) can be divided into two classes. One class of solutions is symmetric with respect to a translation by $\lambda = \dfrac{\pi}{k}$, $u_s(x) = u_s(x + \lambda)$, and the other one is antisymmetric, $u_a(x) = -u_a(x + \lambda)$. $u_s(x)$ corresponds to solutions which are harmonic and $u_a(x)$ which are sub-harmonic with respect to translations $x \to x + \lambda$.

Part of the main effects can be shown again in the limit of long–wavelength modulations in equation (30) ($k \ll q_0$). In this limit equation (29) can be reduced further to an amplitude equation with a spatially varying frequency,

$$\partial_t A = [\varepsilon + iq_0 M_2(x) + 4q_0^2\partial_x^2]A - 3 \mid A \mid^2 A, \tag{32}$$

(i is the imaginary unit). For this derivation we employed the multiple scale ansatz $u = A\exp(iq_0x) + cc$, where $A(x,t)$ and $M(x)(\approx O(\varepsilon))$ are slowly varying on the length scale $2\pi/q_0$ ($k \approx O(\varepsilon^{1/2}q_0)$). Solutions to equation (32) have the same behavior as the starting equation (29), apart from minor differences. Similar generalized GL-equations are expected for systems with comparable broken symmetries. An example is discussed below for Rayleigh-Bénard convection in Section 4.3. According to the relation between equation (29) and the rather general equation (32) the described properties are generic and not specific to the GSH-equation (29) with frustrated drifts. For instance, equations with random frequencies occur extensively in investigations on coupled oscillator systems [23,22].

The first question to be investigated is the bifurcation from the trivial state $u \equiv A \equiv 0$. We do this again with the assumption of small modulation amplitudes $M_2(x) \propto \eta$ and expand the field $A(x)$, the control parameter ε and the frequency ω with respect to powers of η:

$$\varepsilon_c = \varepsilon_c^{(0)} + \eta\varepsilon_c^{(1)} + \eta^2\varepsilon_c^{(2)} + \dots, \tag{33}$$

$$\omega_c = \omega_c^{(0)} + \eta\omega_c^{(1)} + \eta^2\omega_c^{(2)} + \dots, \tag{34}$$

$$A(x) = A_0(x) + \eta A_1(x) + \eta^2 A_2(x) + \dots \tag{35}$$

With the definition,

$$\mathcal{L}_0 = \varepsilon_c^{(0)} + 4q_0^2\partial_x^2, \tag{36}$$

this leads to the hierarchy of equations:

$$\eta^0: \ \mathcal{L}_0 A_0 = 0, \tag{37}$$

$$\eta^1: \ \mathcal{L}_0 A_1 = -[i\bar{M}_2(x) + \varepsilon_c^{(1)} + i\omega_c^{(1)}]A_0, \tag{38}$$

$$\eta^2: \ \mathcal{L}_0 A_2 = -[i\bar{M}_2(x) + \varepsilon_c^{(1)} + i\omega_c^{(1)}]A_1 - [\varepsilon_c^{(2)} + i\omega_c^{(2)}]A_0. \tag{39}$$

In the following we only discuss explicitly the case of a single periodic modulation (30). There are harmonic (symmetric) and subharmonic (antisymmetric) solutions with respect to the modulation $M_2(x)$. Accordingly, we start in the perturbation hierarchy either with constant (harmonic) solution, $A_0 = const.$, or with a subharmonic one, $A_0 \propto \cos(kx)$.

Harmonic solutions

In this case, we start the expansion with $A_0 = constant$ and therefore $\varepsilon_c^{(0)} = 0$ follows from the marginal stability condition. If the solution $B_1(x)$ is periodic, then the integral of (38) over a whole period $2\pi/k$ vanishes. From this solubility condition, we obtain $\varepsilon_c^{(1)} = \omega_c^{(1)} = 0$ and for $\bar{M}_2(x) = 2\bar{G}_2\cos(2kx)$ (with $G_2 = \eta\bar{G}_2$),

$$A_1 = \frac{iq_0}{16q_0^2k^2}\,\bar{M}_2(x)A_0. \tag{40}$$

Also, the integral of (39) over a whole period $2\pi/k$ vanishes which leads to the threshold condition

$$\varepsilon_{h,c}(G_2,k) = \frac{G_2^2}{8k^2} + O(G_2^4), \qquad \omega_c = 0. \tag{41}$$

$\omega_c = 0$ means that there is a stationary bifurcation from $A \equiv 0$ for the branch of harmonic solutions. The modulation $iM_2(x)$ increases the threshold, whereas modulations of the control parameter, $\varepsilon + \xi(x)$, reduce the threshold as shown in the previous Section 4.1.1.

Subharmonic solutions

To describe the subharmonic solutions, the expansion (35) has to be started with

$$A_0 = F_1\exp[ikx] + F_{-1}\exp[-ikx]. \tag{42}$$

The marginal stability condition, $\mathcal{L}_0A_0 = 0$, gives with $\varepsilon_c^{(0)} = 4q_0^2k^2$ a higher threshold than for the harmonic case above. One has now for the subharmonic solutions $\mathcal{L}_0\exp[\pm ikx] = 0$, and therefore the coefficients of

$\exp[\pm ikx]$ on the rhs of equation (38) have to vanish. This requires

$$\varepsilon_c^{(1)} = 0, \qquad \omega_c^{(1)} = \pm \bar{G}_2\, q_0. \tag{43}$$

The solution at next order is

$$A_1(x) = \frac{i\bar{G}_2}{32 q_0 k^2}\left[F_1 e^{3ikx} + F_{-1} e^{-3ikx}\right]. \tag{44}$$

On the rhs of equation (39) the coefficients of $\exp[\pm ikx]$ have to vanish too, which allows the determination of $\varepsilon_c^{(2)} = \bar{G}_2^2/32k^2$. The threshold and the Hopf-frequency up to leading order are

$$\varepsilon_{s,c}(G_2, k) = 4q_0^2 k^2 + \frac{G_2^2}{32k^2} + O(G_2^4), \tag{45}$$

$$\omega_{s,c}(G_2, k) = q_0 G_2 + O(G_2^3). \tag{46}$$

At this subharmonic branch, the imaginary part differs from zero for every finite modulation amplitude G_2. However, the Hopf-bifurcation of the subharmonic branch is only relevant when its threshold drops below the threshold of the harmonic branch, *cf.* equation (41).

Codimension-2 bifurcation

Comparing the thresholds for the harmonic branch, equation (41), and the subharmonic branch, equation (45), it is easy to see that the $\varepsilon_{h,c}$ grows faster with G_2 than $\varepsilon_{s,c}$ and crosses $\varepsilon_{s,c}$ at some critical value $G_{2_{CTP}}$. Then the subharmonic Hopf-bifurcation has the lower threshold. At the critical value $G_{2_{CTP}}$,

$$G_{2_{CTP}} = q_0 k^2 \sqrt{\frac{128}{3}},$$

$$\omega_{CTP} = q_0^2 k^2 \sqrt{\frac{128}{3}}, \tag{47}$$

where the threshold of the harmonic and the subharmonic branch coincide, *i.e.*, one has a codimension-2 point (CTP). Both instabilities compete at this point and the nonlinear interaction between both modes determines which mode survives. For increasing values of G_2, the threshold of the subharmonic Hopf-bifurcation becomes lower than that of the stationary harmonic solutions, which is a surprising result described earlier in a short note [45].

To point out that a periodic modulation $M_2(x)$ has a different consequence for a homogeneous bifurcation than for a periodic bifurcation, we discuss for completeness the generalized real Ginzburg-Landau equation:

$$\partial_t u = \left[\varepsilon + \partial_x^2 + M_2(x)\partial_x\right] u - u^3. \qquad (GGL) \tag{48}$$

With $M_2(x) = 0$, this equation has spatially homogeneous solutions. For spatially harmonic modulation, $M_2(x)$, the drifts in this equation are frustrated as well. However, in equation (48) the frustration does not lead to a Hopf bifurcation. Hence the interplay of a spatially harmonic drift, $M_2(x)$, and a periodic solution, such as in equation (29), is crucial for the phenomenon *Hopf bifurcation by frustrated drifts*. This phenomenon is also relevant for coupled oscillator systems with randomly varying frequencies [4,23,47,48], but it will only occur when the phase approximation, usually employed for coupled oscillator systems, is dropped.

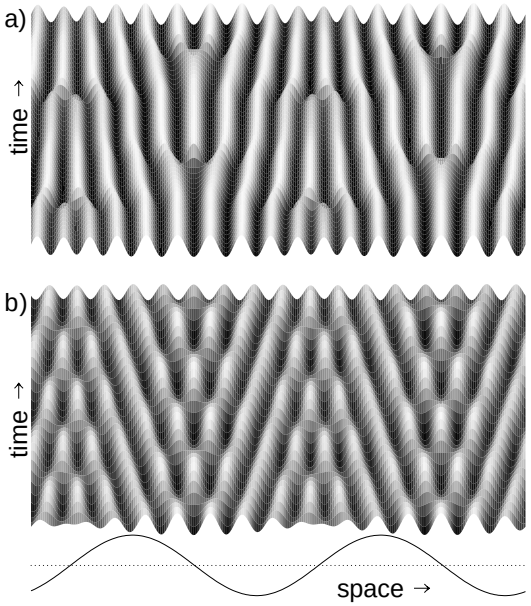

Fig. 12. The solution $u(x,t)$ of the GSH-equation (29) is shown above a Hopf bifurcation as function of space and time for a single periodic drift. In (b) the solution is given just above threshold at $\varepsilon = 0.024$, whereas the threshold value for the Hopf bifurcation is at $\varepsilon = 0.0224\ldots$ In (a) the solution is shown at $\varepsilon = 0.340$, just below the secondary bifurcation into the stationary solution. The modulation amplitude was fixed at $G_2 = 0.03$, and the modulation wave number at $k = q_0/16$. $M_2(x)$ is plotted at the bottom.

If the wave number of $M_2(x)$ is of the order of q_0, the behavior of the GSH-equation (29) and the GGL-equation (48) is changed in a similar manner as for a modulation, $M_1(x)$, of the control parameter ε – only the threshold is shifted. If the modulation wave-number k is much smaller than q_0, say $k < q_0/5$, then a periodically modulated part of the control parameter $M_1(x)$ and a periodic drift $M_2(x)$ lead to qualitatively different behavior of the GSH-equation (29) and periodic patterns in general.

We next describe the typical spatiotemporal behavior beyond a Hopf bifurcation by frustrated drifts. In Figure 12a spatially modulated standing waves are shown, which occur immediately beyond the bifurcation for a single periodic modulation $M_2(x) = 2G_2\cos(2kx)$ with parameters $\varepsilon = 0.05$, $G_2 = 0.05$, and $k = q_0/16$. With increasing ε, the temporal behavior of the solution at each space point becomes more and more anharmonic as shown in Figure 12b. This anharmonicity in the time dependence takes place especially near the secondary bifurcation back to the stationary solution which is stable at larger values of ε.

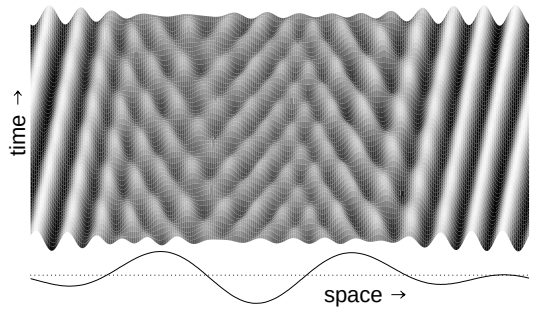

Fig. 13. The solution $u(x,t)$ of the GSH-equation (29) is shown above a Hopf bifurcation as function of space and time and for a doubly periodic drift $M_2(x) = 2G_1\cos[2kx+\pi/2] + 2G_2\cos[3kx+\pi/4]$. $M_2(x)$ is plotted at the bottom.

A doubly periodic drift term $M_2(x) = 2G_2\cos(2kx+\pi/2)+2G_3\cos(3kx+\pi/4)$ leads, instead of standing waves, to aperiodic and chaotic motion as indicated in Figure 13 for the parameters: $G_2 = 0.045$, $G_3 = 0.046$, $k = q_0/16$ and $\varepsilon = 0.068$). More details are given in reference [46].

Essential for the occurrence of the Hopf bifurcation by frustrated drifts is the interplay between the periodic instability and the spatially periodic drift (spatially periodic frequency), whereas the wavelength of the periodic drift is much larger than that of the instability ($k \ll q_0$). The similarities of equation (32) with model equations for coupled oscillator families [47,4], especially for a random function $M_2(x)$, is obvious and will be discussed elsewhere.

4.3 Modulated Rayleigh-Bénard convection

The phenomenon of Hopf bifurcation by frustrated drifts as discussed for models in Section 4.2 can be found in Rayleigh-Bénard convection too. According to detailed calculations described in reference [44] this can occur for instance for a wavy top boundary and a simultaneous temperature modulation at the bottom boundary as indicated in Figure 14. The undulated top boundary maybe located at $z = d(1+H_0)$, with $H_0 = F_0\cos(k_0x)$ and the temperature maybe modulated at the bottom boundary ($z=0$), as $T_b = \bar{T}_b + H_2(x)(\bar{T}_b - T_u)/R_c^f$, with the dimensionless modulation function $H_2(x) = F_2\cos(k_2x+\varphi_2)$ and $R_c^f = 27\pi^4/4$. These modulations at the top and bottom boundary then lead to an oscillatory bifurcation from a primary state. Such a Hopf–bifurcation by frustrated drifts takes place for various combinations of the modulation amplitudes F_i and the modulation wave numbers k_i [44,49]. An example is $k_2/k_0 = 2$, $\varphi_2 = \pm\pi$ and the amplitudes F_i beyond a critical threshold [44].

For such an experimental design and for small modulation amplitudes it is also possible to derive an equation for the envelope $A_0(x,t)$ of thermal convection

$$\mathbf{u}(x,z,t) = \Big[A_0e^{iq_cx} + A_0^*e^{-iq_cx}\Big]\mathbf{U}_0(z) \qquad (49)$$

by using a well established perturbation scheme [4,50,51]. Herein the vector $\mathbf{u}$ contains the temperature field and the velocity potential as components and q_c is the critical wave number at onset of convection. For the expansion, one uses as a small parameter $\varepsilon = (\Delta T - \Delta T_c)/\Delta T_c$, which measures the distance from the critical temperature difference at convective onset in the unmodulated case. Assuming additionally small modulation wave numbers, $(k/q_c) \propto \varepsilon^{1/2}$ and $H_i(x) \propto \varepsilon^{1/2}$, one can derive for this modulated convection cell, as shown in Figure 14, a generalized amplitude equation of the form [52],

$$\begin{aligned}\tau_0\partial_tA_0 = \Big[&\varepsilon - \frac{7}{3}H_0^2 + 3H_0 + \Big(1+\frac{5}{3}H_0\Big)\frac{H_2}{R_c}\\ &+ i\frac{\sqrt{2}}{\pi}\Big(\frac{271}{576}\partial_xH_0 - \frac{5}{192R_c}\partial_xH_2\Big)\Big]A_0\\ &+ \Big[i\frac{2\sqrt{2}}{3\pi}\Big(H_0 - \frac{1}{R_c}H_2\Big)\partial_x + \xi_0^2\partial_x^2 - \alpha \mid A_0\mid^2\Big]A_0,\end{aligned} \qquad (50)$$

with $\xi_0^2 = \alpha = 8/3\pi^2$ and $\tau_0 = 9\pi^2/2R_c$. Here the coefficients in the equation are calculated for stress–free boundary conditions, but they have been determined for realistic boundary conditions too [46].

An analysis of the linear part of equation (50), as well as a full analysis of the Navier-Stokes equations [44] shows that by raising the modulation amplitudes in Rayleigh-Bénard convection, the onset of a spatially periodic convection pattern can be changed *via* Hopf bifurcation by frustrated drifts from a stationary to an temporarily oscillating one. There is good agreement between results obtained by starting from the full equations and the amplitude equation (50) [44,49]. Similar as for the Swift-Hohenberg equation in (29), immediately above the Hopf bifurcation by frustrated drifts, standing waves instead of traveling waves are the preferred and stable solutions. With increasing values of the control parameter, the solutions of (50) become at first aperiodic and then spatiotemporal complex, before a regime of very slowly traveling waves is reached at large values of ε [49].

Traveling waves are known in binary fluid mixtures and in electroconvection. In both systems traveling waves bifurcate subcritically (discontinuous) and perturbation

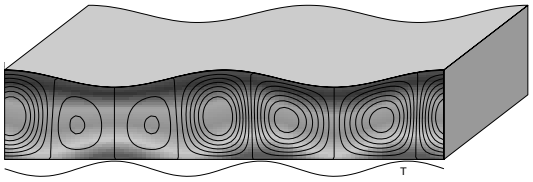

Fig. 14. An experimental design for modulated Rayleigh-Bénard Convection with a combination of an upper plate of corrugated form and a temperature modulation at the lower plate. The ratio of the wave numbers of the periodic undulation of the top plate (k_0) and the temperature modulation at the bottom plate (k_2) is k_0: $k_2 = 2:3$. The gray scale in the fluid layer indicates the temperature field of the primary flow, and along the solid lines the velocity potential of the primary flow is constant [44]. The curve below the cell indicates the temperature variation at the bottom plate.

methods cannot be applied for the determination of the nonlinear solutions behavior. Since the nonlinear coefficient, α, in equation (50) is left unchanged by small modulations at boundaries, the Hopf bifurcation by frustrated drifts occurring in modulated thermal convection is supercritical as well. This justifies the application of perturbation methods for the characterization of the nonlinear solutions.

4.4 Conclusion

We have shown that heterogeneities reduce the symmetry and thereby induce a number of interesting phenomena in pattern forming systems, such as localization of wave pattern, cellular patterns, semi-log scaling and dynamical states *via* a Hopf-bifurcation by frustrated drifts.

So far examples have been studied where heterogeneities modify the bifurcation from a trivial basic state to a spatially periodic pattern. Another interesting question is how heterogeneities modify the bifurcation to traveling waves or to spatio-temporal chaotic patterns, such as Spiral–Defect–Chaos in thermal convection [53,54]. In the latter system, the reduced symmetry may lead for instance to new frozen patterns and surprising domain–wall patterns.

The Hopf bifurcation by frustrated drifts shows that broken symmetries related to inhomogeneities also allow a controlled modification of the bifurcation type, for example, a change from a stationary bifurcation to an oscillatory bifurcation or even to spatio–temporal complex behavior.

An additional feature, which is also seen in porous media convection and in Taylor vortices flow: the presence of spatial randomness suppresses the higher order instabilities, *i.e.* wavy Taylor–Vortex–Flow or in the case of PMC, cross rolls or similar 3D structures. These and a number of similar questions not touched so far are addressed in future works.

Part of this work was done during fruitful collaborations with Lawrence Howle, Rainer Schmitz, Mark Shattuk and Mark Steen. The work of RPB and BP was supported by the US NSF under grant number CTS-9610248 and the work of WZ was supported by the DFG.

References

1. *Propagation in Systems far from Equilibrium*, edited by J.E. Wesfreid *et al.* (Springer, New York, 1988).
2. *Nonlinear Evolution of Spatio-Temporal Structures in Dissipative Continuous Systems*, edited by F.H. Busse, L. Kramer (Plenum Press, New York, 1990).
3. *Pattern Formation in Complex Dissipative Systems*, edited by S. Kai (World Scientific, Singapore, 1992).
4. M.C. Cross, P.C. Hohenberg, Rev. Mod. Phys. **65**, 851 (1993).
5. *Spatio-Temporal Patterns in Nonequilibrium Complex Systems*, Vol. XXI of *Santa Fe Institute Studies in the Sciences of Complexity*, edited by P. Cladis, P. Palffy-Muhoray (Addision-Wesley, New York, 1995).
6. F.H. Busse, in *Hydrodynamic Instabilities and the Transition to Turbulence*, Vol. 45 of *Topic in Applied Physics*, edited by H.L. Swinney, J.P. Gollub (Springer, New York, 1986).
7. R.C. DiPrima, H.L. Swinney, in *Hydrodynamic Instabilities and the Transition to Turbulence*, *Topic in Applied Physics*, edited by H.L. Swinney, J.P. Gollub (Springer, New York, 1981), p. 139.
8. W. Zimmermann, Mat. Res. Bulletin **16**, 46 (1991).
9. L. Kramer, W. Pesch, Annu. Rev. Fluid Mech. **27**, 515 (1995).
10. D.A. Nield, A. Bejan, *Convection in Porous Media* (Springer, Berlin, 1991).
11. I.M. Lifshitz, S.A. Gredeskul, L.A. Pastur, *Introduction to the Theory of Disordered Systems* (Wiley, New York, 1988).
12. P.W. Anderson, Phys. Rev. **109**, 1492 (1958).
13. Y.S. Kivshar, S.A. Gredeskul, A. Sanchez, L. Vázquez, Phys. Rev. Lett. **64**, 1693 (1990).
14. W. Zimmermann, M. Sesselberg, F. Petruccione, Phys. Rev. E **48**, 2699 (1993).
15. M. Lowe, J.P. Gollub, T. Lubensky, Phys. Rev. Lett. **51**, 786 (1983).
16. M. Lowe, B.S. Albert, J.P. Gollub, J. Fluid Mech. **173**, 253 (1986).
17. P. Coullet, Phys. Rev. Lett. **56**, 724 (1986).
18. P. Coullet, L. Gil, D. Repaux, in *Instabilities and Nonequilibrium Structures II*, edited by E. Tirapequi, D. Villaroel (Kluwer, Dordrecht, 1987), pp. 189–205.
19. P. Coullet, D. Walgraef, Europhys. Lett. **10**, 525 (1989).
20. W. Zimmermann *et al.*, Europhys. Lett. **24**, 217 (1993).
21. A. Ogawa, W. Zimmermann, K. Kawasaki, T. Kawakatsu, J. Phys. II France **6**, 305 (1996).
22. Y. Kuramoto, Prog. Theor. Phys. **94**, 321 (1995).
23. G.B. Ermentrout, Physica (Nonlinear Phenomena) D **41**, 219 (1990).
24. P. Carpenter, Nature **388**, 713 (1997); L. Sirovich, S. Karlsson, Nature **388**, 753 (1997).
25. L. Howle, R.P. Behringer, J. Georgiades, Nature **362**, 230 (1993).
26. M.D. Shattuck, R.P. Behringer, G.A. Johnson, J.G. Georgiadis, J. Fluid Mech. **332**, 215 (1997).
27. L. Howle, R.P. Behringer, J.G. Georgiadis, J. Fluid Mech. **332**, 247 (1997).
28. B. Painter, R. Behringer *Effects of spatial disorder on the transition to Taylor-Vortex Flow* (to be published).
29. D.S. Cannell, M.A. Dominguez-Lerma, G. Ahlers, Phys. Rev. Lett. **50**, 1365 (1983).
30. I. Rehberg, E. Bodenschatz, B.Winkler, F.H. Busse, Phys. Rev. Lett. **59**, 282 (1987).
31. R.E. Kelly, D. Pal, J. Fluid Mech. **86**, 433 (1978).
32. G. Hartung, F.H. Busse, I. Rehberg, Phys. Rev. Lett. **66**, 2741 (1991).
33. J. Herrmann, F.H. Busse, J. Fluid Mech. **350**, 209 (1997).
34. P. Coullet, P. Huerre, Physica (Nonlinear Phenomena) D **23**, 27 (1986).
35. J. Tavantzis, E.L. Reiss, B.J. Matkowsky, SIAM J. Appl. Math. **34**, 322 (1978).
36. L. Kramer, H. Riecke, Z. Physik B **59**, 245 (1985).
37. C. Braester, P. Vadasz, J. Fluid Mech. **254**, 345 (1993).

38. N.J. O'Sullivan, R. McKibbin, Transport Porous Media **1**, 293 (1986).
39. D.A.S. Rees, D.S. Riley, J. Fluid Mech. **199**, 133 (1989).
40. D.A.S. Rees, D.S. Riley, Proc. R. Soc. London A **421**, 303 (1989).
41. P. Vadasz, C. Braester, Acta Mechanica **91**, 215 (1992).
42. J.B. Swift, P.C. Hohenberg, Phys. Rev. A **15**, 315 (1977).
43. P. Coullet, D. Repaux, Europhys. Lett. **3**, 573 (1987).
44. R. Schmitz, W. Zimmermann, Phys. Rev. E **53**, 5993 (1996).
45. W. Zimmermann, R. Schmitz, Phys. Rev. E **53**, R1321 (1996).
46. W. Zimmermann, Degenerated Hopf-bifurcation and chaos induced by frustrated drifts, submitted to Physica D, 1998.
47. P.C. Matthews, R.E. Mirollo, S.H. Strogatz, Physica (Nonlinear Phenomena) D **52**, 293 (1991).
48. N. Nakagawa, Y. Kuramoto, Physica (Nonlinear Phenomena) D **80**, 307 (1995).
49. R. Schmitz, W. Zimmermann, submitted to J. Fluid Mech., 1998.
50. A.C. Newell, J.A. Whitehead, J. Fluid Mech. **38**, 279 (1969).
51. A.C. Newell, T. Passot, J. Lega, Annu. Rev. Fluid Mech. **25**, 399 (1992).
52. W. Zimmermann, *Effects of Inhomogeneities in Pattern Formation, Habilitationsschrift, RWTH Aachen* (unpublished), 1994.
53. S.W. Morris, E. Bodenschatz, D.S. Cannell, G. Ahlers, Phys. Rev. Lett. **71**, 2036 (1993).
54. M. Assenheimer, V. Steinberg, Phys. Rev. Lett. **70**, 3888 (1993).